materials

MDPI

Article

Magnetic Field-Assisted Photocatalytic Degradation of Organic Pollutants over $Bi_{1-x}R_xFeO_3$ (R = Ce, Tb; x = 0.00, 0.05, 0.10 and 0.15) Nanostructures

Radhalayam Dhanalakshmi [1,*], Nambi Venkatesan Giridharan [2] and Juliano C. Denardin [1,*]

[1] Physics Department and CEDENNA, University of Santiago of Chile (USACH), Santiago 9170124, Chile
[2] Advanced Functional Materials Laboratory, Department of Physics, National Institute of Technology, Tiruchirappalli 620015, TN, India; giri@nitt.edu
* Correspondence: dhanalakshmi.radhalayam@usach.cl (R.D.); juliano.denardin@usach.cl (J.C.D.)

Abstract: Magnetic-field-accelerated photocatalytic degradation of the phenol red (PR) as a model organic pollutant was studied using rare-earth elements modified $BiFeO_3$ ($Bi_{1-x}R_xFeO_3$ (R = Ce, Tb; x = 0.0, 0.05, 0.10 and 0.15); BFO: RE) nanostructures. The nanostructures were prepared via the hydrothermal process and their morphological, structural, functional, optical and magnetic features were investigated in detail. The effect of magnetic fields (MFs) on photocatalysis were examined by applying the different MFs under visible light irradiation. The enhanced photodegradation efficiencies were achieved by increasing the MF up to 0.5T and reduced at 0.7T for the compositions x = 0.10 in both Ce and Tb substituted BFO. Further, mineralization efficiencies of PR, reproducibility of MF-assisted photocatalysis, stability and recyclability of BFO: RE nanostructures were also tested.

Keywords: $BiFeO_3$; hydrothermal; nanostructures; photocatalysis; phenol red; magnetic field

Citation: Dhanalakshmi, R.; Giridharan, N.V.; Denardin, J.C. Magnetic Field-Assisted Photocatalytic Degradation of Organic Pollutants over $Bi_{1-x}R_xFeO_3$ (R = Ce, Tb; x = 0.00, 0.05, 0.10 and 0.15) Nanostructures. *Materials* **2021**, *14*, 4079. https://doi.org/10.3390/ma14154079

Academic Editor: Dimitrios Papoulis

Received: 27 June 2021
Accepted: 20 July 2021
Published: 22 July 2021

1. Introduction

Over the last decades, Bismuth ferrite (BFO) is one of the most efficient and promising materials that have gained much attention in modern scientific research because of its great prospect in resolving energy and environmental issues [1,2]. It was established as an attractive visible light photocatalyst due to its narrow bandgap (2.1 eV), advanced magnetic properties, excellent chemical stability, low cost and non-toxic [3–5]. BFO has been considered as an alternative for efficiency limits compared to widely used photocatalytic materials TiO_2 and ZnO since these can only absorb ultraviolet light, which occupies only 4% of the whole solar energy [6,7]. The strong oxidation and reduction capabilities (1.74 V (vs. NHE) and −0.39 V (vs. NHE), respectively, [8]) of BFO can be used to convert light energy into different energy types and make changes in organic azo dyes such as phenol red. Phenol red ($C_{19}H_{14}O_5S$) [9,10] is one of the groups of organic phenol dye (standard reduction potential value of 0.35V (vs. SCE) [11,12]), belongs to the family of triphenylmethane dyes. These are extremely brilliant and intensely colored synthetic organic dyes, used in the paper, textile industries, in the coloring of a large variety of products, as well as in the analytical and medical sectors because they can provide the whole coloration range [13]. These compounds are present in a high number of colored industrial wastewaters that are released into the environment. PR is one of harmful dye, which is widely used in chemical laboratories as a pH indicator, estrogenic properties and screening test. Despite its applications, toxicology information reveals that contact or prolonged exposure to PR may produce skin and eyes damage, irritation with redness and pain. The PR inhalation can cause irritation to the respiratory tract, and ingestion can affect the gastrointestinal tract. Hence, the choice of phenol red dye removal by BFO is of enormous value. However, BFO in its pure form shows low photocatalytic efficiency due to its rapid recombination of charge carriers. In this aspect, many strategies have been

developed for improving photocatalytic efficiencies, such as doping with rare-earth (RE) elements [14], making heterojunctions, metal loading etc. Despite of these approaches, retarding the high recombination rate of photo-generated carriers is one of the effective approaches to enhance the catalytic performance. This could be realized by coupling photocatalysis with various external energy fields. Recently, photocatalytic efficiency has been significantly enhanced by using the external electric field [15–17] to the photocatalysis. For instance, an oriented electric field accelerates the non-redox, bond-forming process of Diels-Alder reaction [18] and evolves an opportunity of precise manipulation of chemical reaction. The catalytic activity of platinum can also tune by elastic strain in a regulated and predictable way [19,20]. In the similar way microwave [21,22], ultrasonic fields [23,24], low-temperature plasma [25,26] and magnetic fields (MFs) [27] have been used to acquire the beneficial effect on photocatalysis both for duration and efficiency. Among these, a MF-assisted photocatalytic process has been put forward to control the photo-induced hole and electron recombination, which is similar to the electron transfer reactions. Therefore, by considering the resemblances between photocatalytic and electron transfer reactions, the utilization of MFs to raise the photocatalytic efficiency, i.e., the effect of external MFs on chemical reactions is the MF-assisted photocatalytic activity [27,28], which is an environment-friendly method, and has been extensively discussed and efficiently contributed towards sustainable advancements [29].

BFO exhibits the coexistence of ferroelectric and magnetic order in the same phase. It has the rhombohedral distorted ABO_3 type perovskite structure and possesses the G-type antiferromagnetism including cycloidal spin structure [30]. The enhanced magnetic properties of RE substituted BFO suppress its cycloidal spin structure, would affect the magnetic-field assisted photocatalytic activity of the BFO nanostructures [31]. An applied external MF may change the possible reaction probability and the movement of the charged species by magnetically induced retarding of electron-hole recombination [28]. However, the strength of the MF affects the recombination rate of the photo-generated radicals [32]. Strong MFs up to several kOe have been used for noticeable improvements in photocatalytic responses using TiO_2 and ZnO catalysts. Wakasa et al. investigated the MF effects on photodegradation of tert-butyl alcohol with platinized TiO_2 particles under 0–1.5T of an external MF [33]. Lately, an enhancement in the photocatalytic behavior of ZnO by applying the MFs were studied by Okumura et al. [34]. The enhanced photocatalytic activity observed through MF boosting carrier transport in α-Fe_2O_3/rGO [35]. However, to the best of our knowledge, the comparative studies on the MF-assisted photocatalytic activity of RE-substituted BFO (BFO: RE) under different field strengths towards the degradation of organic pollutant phenol red have not yet been made. In this work, we chosen the cerium and terbium as a model RE elements to investigate the MF-accelerated photocatalytic behavior of BFO. The hydrothermal process has been adapted to prepare the $Bi_{1-x}R_xFeO_3$ (R = Ce, Tb; x = 0.00, 0.05, 0.10 and 0.15) nanostructures and studied their various properties. The enhanced MF-accelerated photocatalytic activity of $Bi_{1-x}R_xFeO_3$ (R = Ce, Tb; x = 0.00, 0.05, 0.10 and 0.15) nanostructures were investigated by applying the different external MFs towards the degradation of PR in visible-light illumination. In order to evaluate the reproducibility of heterogeneous MF-assisted photocatalysis and stability of catalysts, the recyclable tests were also studied.

2. Materials and Methods

The $Bi_{1-x}R_xFeO_3$ (R = Ce, Tb; x = 0.00, 0.05, 0.10 and 0.15) nanostructures were synthesized at 200 °C by hydrothermal process [36,37] by using bismuth nitrate [Bi $(NO_3)_3{\cdot}5H_2O$], iron nitrate [Fe $(NO_3)_3.9H_2O$], cerium nitrate [$CeN_3O_9{\cdot}6H_2O$] and terbium nitrate [Tb $(NO_3)_3{\cdot}6H_2O$] as precursors. The size and morphology of the prepared nanostructures were investigated using HR-TEM (Jeol 2010, Jeol, Tokyo, Japan). The purity and crystallinity of the samples were examined by X-ray diffractometry (XRD) on a (D/MAX Ultima III, Rigaku Corporation, Tokyo, Japan) with CuKα radiation. Fourier transform infrared (FT-IR) spectroscopy (Perkin Elmer/spectrum RXI, Perkin Elmer, Texas City, TX, USA) was

used to evaluate the local structure of the samples. The optical studies of prepared nanostructures were conducted on a UV-visible diffuse reflectance spectrophotometer (JASCO Model V-670, Jasco, Easton, MD, USA). The magnetic properties of prepared samples were studied through vibrating sample magnetometry (VSM) (Lake Shore-7404 VSM, Lake Shore Cryotronics, Westerville, OH, USA).

The MF-assisted photocatalytic activity of $Bi_{1-x}R_xFeO_3$ (R = Ce, Tb; x = 0.00, 0.05, 0.10 and 0.15) were studied by applying the external MFs of 0.0, 0.3, 0.5 and 0.7T. An electromagnet was used to produce the preferred MF to degrade the 10 ppm of PR (pH 6.7) solution, which is placed in a quartz cell along with 10 mg of the synthesized photocatalyst. Before illumination to the visible light, the solution was stirred for 30 min in dark to attain absorption and desorption equilibrium. The catalytic activities were carried out under the visible light irradiation by a 150 W Xenon lamp (Toption, Toption Instruments, Xian, China) with a cutoff filter for $\lambda \geq 400$ nm (600 mW/cm^2 at wavelength of 650 nm) at room temperature (30–32 °C). After the elapse of known period (for every 15mins), a small quantity of the solution was taken and centrifuged to remove any catalyst in the solution. The concentration of PR was determined by measuring the absorbance at 443 nm using a UV-Vis absorption spectrophotometer (Shimadzu UV-1700, Shimadzu, Kyoto, Japan). The mineralization efficiencies of PR were performed on a total organic carbon Analyzer (Analytikjena/multi-N/C 3100, Analytik Jena, Jena Germany), respectively.

3. Results and Discussion

Figure 1a–f shows the typical HR-TEM images of $Bi_{1-x}R_xFeO_3$ (R = Ce, Tb; x = 0.05, 0.10 and 0.15) nanostructures. The nanostructures were found to have nano-rod-like morphology and seem similar to be agglomerated. The length and diameter of nano-rods were around 16–24 nm and 1.6–3.5 nm for BFO: Ce nanostructures, whereas the length and diameter of nanorods were observed as 20–30 nm and 4–6.5 nm for BFO: Tb nanostructures, respectively.

Figure 1g–l illustrates the lattice fringes corresponding to the $Bi_{1-x}R_xFeO_3$ (R = Ce, Tb; x = 0.05, 0.10 and 0.15), revealed that phase formation occurred with a high order of crystalline nature. The distance between two parallel planes of $Bi_{1-x}Ce_xFeO_3$ (x = 0.05, 0.10 and 0.15) nanostructures were found to be 2.82 Å (110), 3.67 Å (012) and 1.99 Å (024), respectively. For the BFO: Tb nanostructures, the lattice fringe spacing were observed as 1.75 Å (122), 1.62 Å (300) and 1.38 Å (214), respectively, in agreement with interplanar distance estimated from the XRD analysis.

Figure 2a shows the X-ray diffraction patterns of hydrothermally synthesized BFO: RE nanostructures. The diffraction peaks of x = 0.00 corresponds to the rhombohedral (*R3c* space group) of BFO. However, the secondary phase ($Bi_2Fe_4O_9$) is also detected at 27° due to the kinetics of formation. This phase is well suppressed when the concentration of RE elements increased to 5% and 10%, which is consistent with the earlier reports on substitution with a moderate amount of RE ions in place of Bi^{3+} could eliminate the impurity phases in BFO [38–41]. However, by increasing the concentration of Ce and Tb to 15% ($Bi_{0.85}Ce_{0.15}FeO_3$ and $Bi_{0.85}Tb_{0.15}FeO_3$), the presence of the small impurity phases was assigned as the $CeFeO_3$ and $TbFeO_3$, respectively.

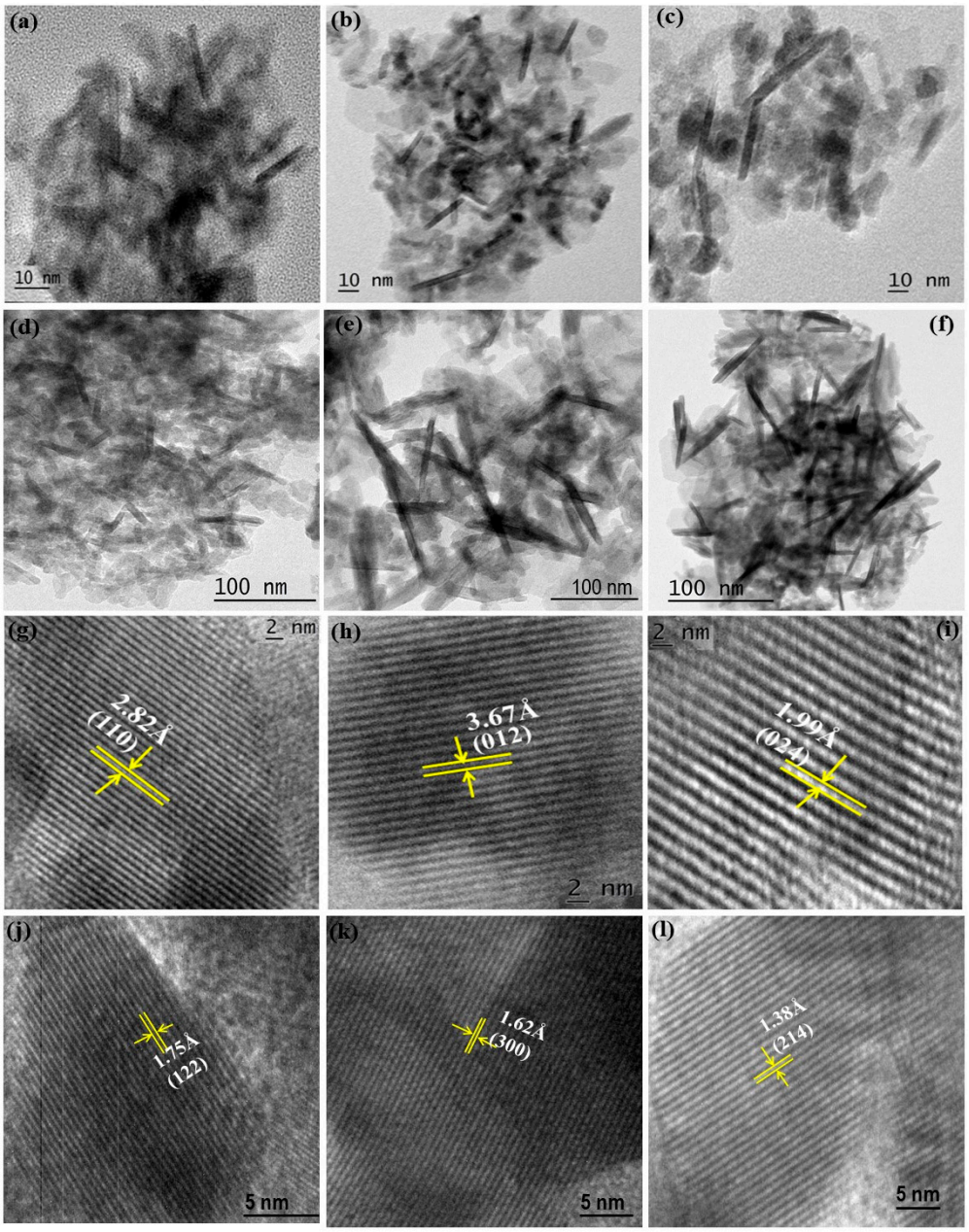

Figure 1. (**a**–**f**) HR-TEM images, (**g**–**l**) lattice fringes for the $Bi_{0.95}Ce_{0.05}FeO_3$, $Bi_{0.90}Ce_{0.10}FeO_3$, $Bi_{0.85}Ce_{0.15}FeO_3$, $Bi_{0.95}Tb_{0.05}FeO_3$, $Bi_{0.90}Tb_{0.10}FeO_3$, $Bi_{0.85}Tb_{0.15}FeO_3$ nanostructures.

Figure 1g–l illustrates the lattice fringes corresponding to the $Bi_{1-x}R_xFeO_3$ (R = Ce, Tb; x = 0.05, 0.10 and 0.15), revealed that phase formation occurred with a high order of crystalline nature. The distance between two parallel planes of $Bi_{1-x}Ce_xFeO_3$ (x = 0.05, 0.10 and 0.15) nanostructures were found to be 2.82 Å (110), 3.67 Å (012) and 1.99 Å (024), respectively. For the BFO: Tb nanostructures, the lattice fringe spacing were observed as 1.75 Å (122), 1.62 Å (300) and 1.38 Å (214), respectively, in agreement with interplanar distance estimated from the XRD analysis.

Figure 2a shows the X-ray diffraction patterns of hydrothermally synthesized BFO: RE nanostructures. The diffraction peaks of x = 0.00 corresponds to the rhombohedral (*R3c* space group) of BFO. However, the secondary phase ($Bi_2Fe_4O_9$) is also detected at 27° due to the kinetics of formation. This phase is well suppressed when the concentration of RE elements increased to 5% and 10%, which is consistent with the earlier reports on substitution with a moderate amount of RE ions in place of Bi^{3+} could eliminate the

impurity phases in BFO [38–41]. However, by increasing the concentration of Ce and Tb to 15% ($Bi_{0.85}Ce_{0.15}FeO_3$ and $Bi_{0.85}Tb_{0.15}FeO_3$), the presence of the small impurity phases was assigned as the $CeFeO_3$ and $TbFeO_3$, respectively.

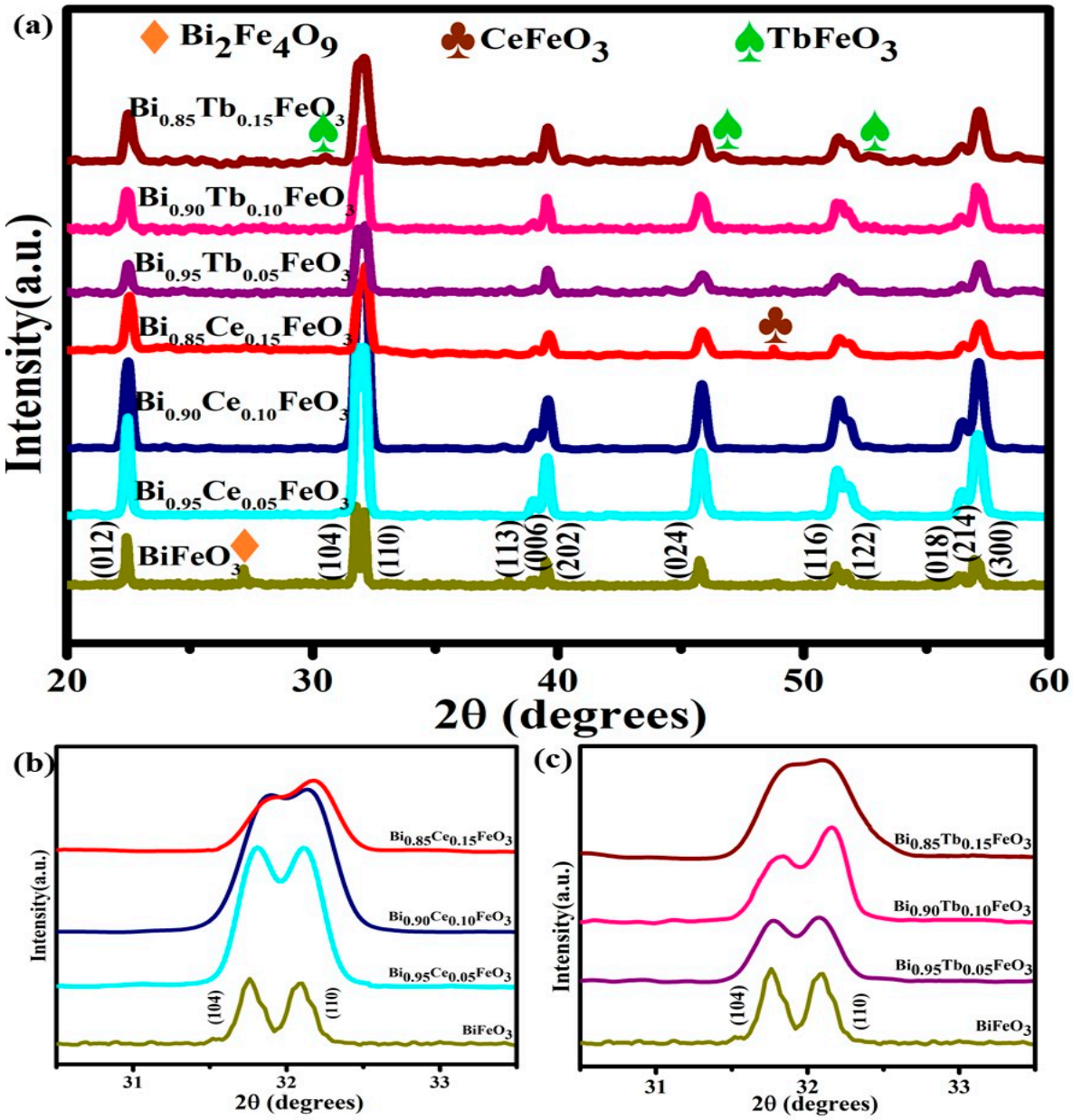

Figure 2. (**a**) XRD patterns of $Bi_{1-x}R_xFeO_3$ (R = Ce, Tb; x = 0.00, 0.05, 0.10 and 0.15) samples synthesized at 200 °C. (**b**) Expanded XRD pattern for the BFO: Ce, (**c**) BFO: Tb samples.

The magnified XRD patterns in the vicinity of 2θ = 32° are shown in Figure 2b,c. By increasing the concentration of RE, rhombohedral peak merging and shifting to the higher angles may reflect the structural transformation from rhombohedral (*R3c*) to orthorhombic ((*Pnma*) and ($Pn2_1a$)) for BFO: Ce and BFO: Tb nanostructures, respectively, which are reliable with the earlier reports [39–41].

The FTIR spectrum BFO: RE nanostructures are illustrated in Figure 3. The broad band between 3000–3600 cm^{-1} arose from the antisymmetric and symmetric stretching of bond H_2O and OH^- groups, while a band at 1592 cm^{-1} corresponded to the bending vibrations of H_2O [42,43]. Bands between 900 and 1410 cm^{-1} are due to the existence of trapped nitrates present in the sample. The presence of a metal-oxygen band can confirm

the formation of the perovskite structure [44]. The formation of FeO_6 octahedra of the perovskite structure by the typical characteristic metal-oxygen bonds between 400 and 600 cm^{-1} in all samples.

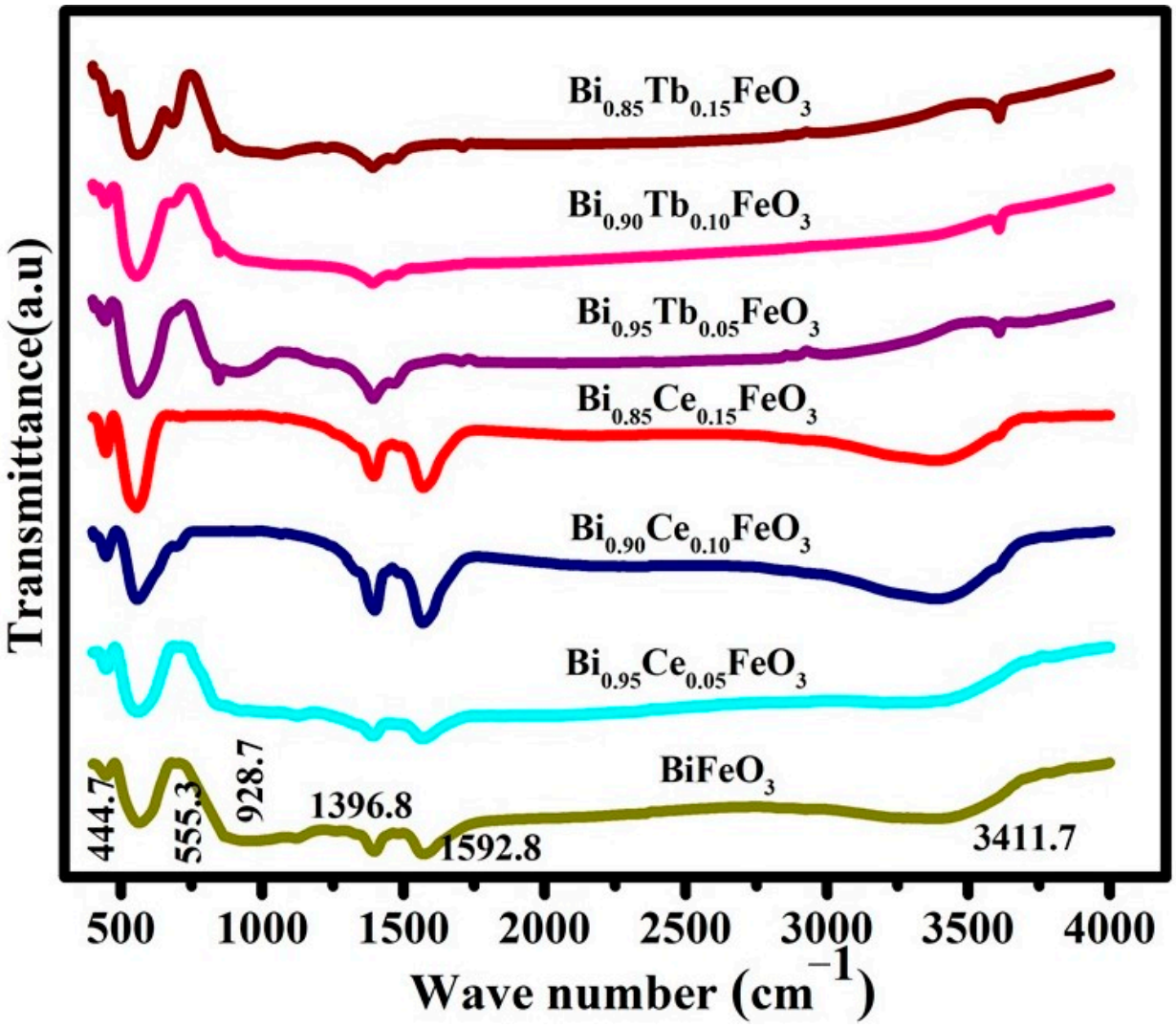

Figure 3. FT-IR spectrum of the as-prepared BFO: RE nanostructures.

The UV–Vis diffuse reflectance spectra (DRS) of $Bi_{1-x}R_xFeO_3$ (R = Ce, Tb; x = 0.00, 0.05, 0.10 and 0.15) nanostructures are shown in Figure 4a,b and the band gaps deduced from Kubelka-Munk function [45]. The nanostructures exhibited a greater absorption in the visible range and the optical bandgap was found to be 2.03 eV [38] for $BiFeO_3$ nanostructures. The observed band-gap energies [1.95, 1.91 and 1.82 eV for $Bi_{1-x}Ce_xFeO_3$ (x = 0.05, 0.10 and 0.15)] are noticeably reduced with an increase of RE concentration. The obtained decreased bandgaps were found to be 2.00, 1.90 and 1.87 eV for the $Bi_{1-x}Tb_xFeO_3$ (x = 0.05, 0.10 and 0.15) nanostructures, respectively.

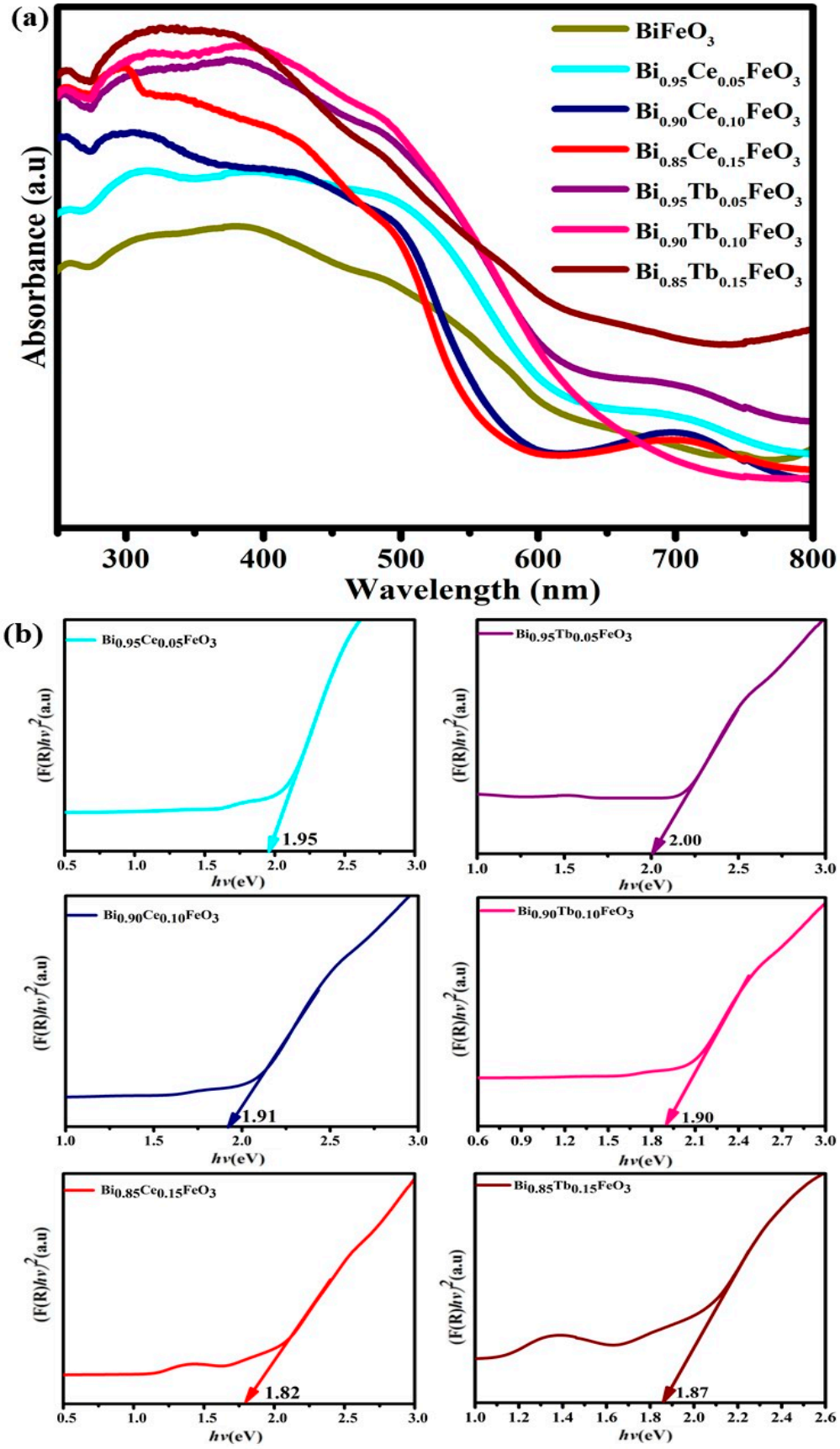

Figure 4. (**a**) DRS spectra of BFO: RE nanostructures. (**b**) $(F(R)hv)^2$ versus photon energy (hv) for the $Bi_{1-x}R_xFeO_3$ (R = Ce, Tb; x = 0.05, 0.10 and 0.15) nanostructures.

The possible reduction in the bandgap could be ascribed to the RE-substitution induced formation of new energy states (defect levels) introduced between the valence band and conduction band [46]. Another perspective is the structural distortion persuaded modification in RE-modified BFO nanostructures. The bond angle variation in Fe-O-Fe due to the RE substitution also results in the reduced band-gap energy. The hybridization between Fe-3d and O-2p, in turn, depends on the Fe-O-Fe exchange angle and any change in the bond angle also alters the bandgap of BFO [46,47]. The narrow band gap values and high absorption in the visible range of BFO: Ce and BFO: Tb nanostructures leads the potential photocatalytic applications.

Figure 5 shows the magnetization-magnetic field (*M-H*) curves of BFO: RE nanostructures at room-temperature. A weak ferromagnetic behavior is observed for the x = 0.00 with spontaneous magnetization (M_s) of 2.28 emu/g. By increasing the concentration of the RE in BFO, spontaneous magnetization was found to increase, exhibited M_s values are 3.33, 3.93, 5.35, 2.94, 3.51 and 5.10 emu/g for $Bi_{0.95}Ce_{0.05}FeO_3$, $Bi_{0.90}Ce_{0.10}FeO_3$, $Bi_{0.85}Ce_{0.15}FeO_3$, $Bi_{0.95}Tb_{0.05}FeO_3$, $Bi_{0.90}Tb_{0.10}FeO_3$ and $Bi_{0.85}Tb_{0.15}FeO_3$, respectively. The observed increment in magnetization for BFO:RE compositions are attributed to small particle size, a net magnetic moment of chosen RE element and the structural distortion [40,48].

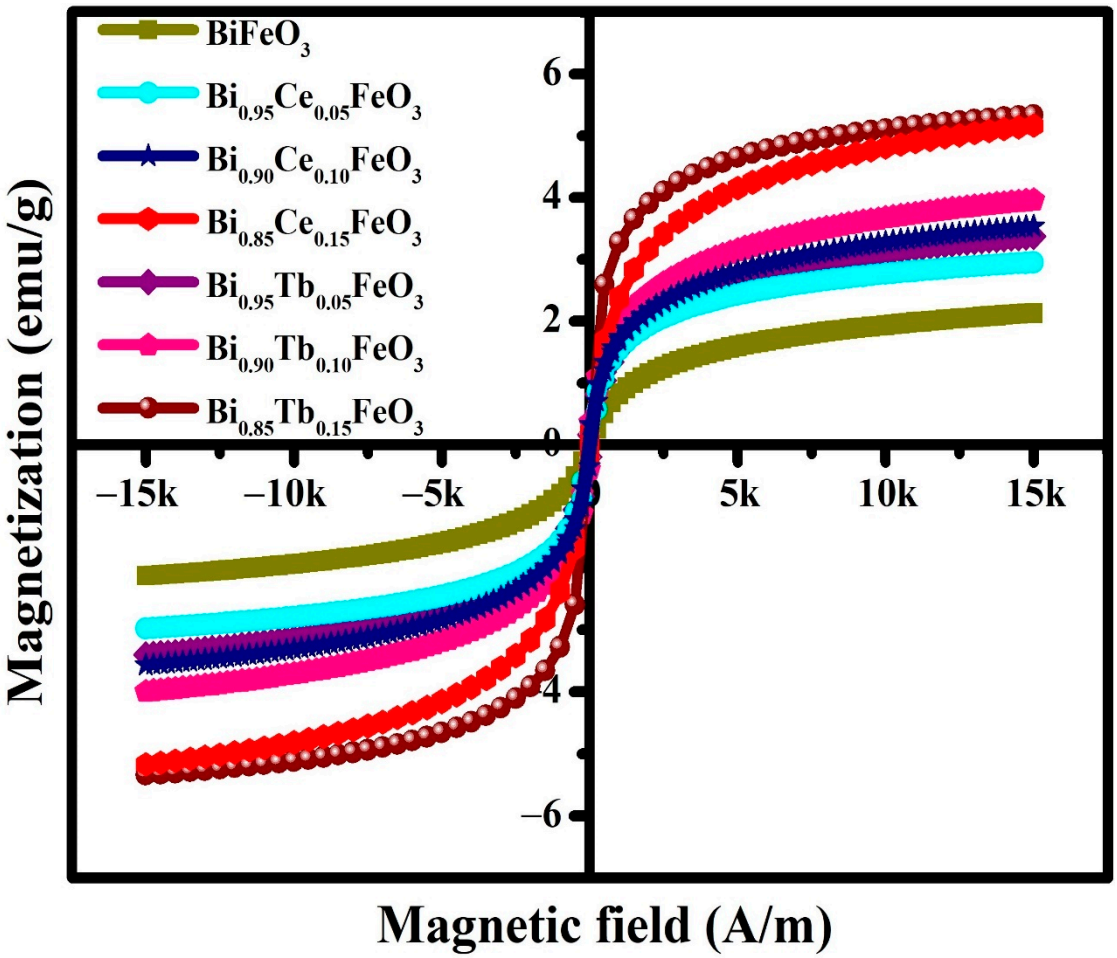

Figure 5. Magnetization (*M*) versus field (*H*) hysteresis loops for the prepared BFO: RE, measured at 300 K.

The photocatalytic degradation capabilities of PR over BFO: RE in the absence and presence of MFs (0.0, 0.3, 0.5 and 0.7T) under visible light illumination are shown in Figure 6a–d and summarized in Table 1. At the end of 90 min, the improved photodegradation efficiencies (35.2, 50.2, 81.3, 69.1, 43.7, 75.7 and 65.1% for $BiFeO_3$, $Bi_{0.95}Ce_{0.05}FeO_3$, $Bi_{0.90}Ce_{0.10}FeO_3$, $Bi_{0.85}Ce_{0.15}FeO_3$, $Bi_{0.95}Tb_{0.05}FeO_3$, $Bi_{0.90}Tb_{0.10}FeO_3$ and $Bi_{0.85}Tb_{0.15}FeO_3$,

respectively) are observed by increasing the RE content (Figure 6a). The degradation efficiencies increase with rising the RE concentration in BFO except for x = 0.15, and the highest efficiency was noticed for x = 0.10 in all the cases. This can be understood by doping the RE elements to BFO increases space-charge width near the phase boundary, that increases the number of separated electron and holes leads an enhanced photocatalytic activity [49]. The photocatalytic efficacies were increased gradually by applying the external MF. By applying the external MFs of 0.3T, the improved photodegradation ability have been observed for the compositions $Bi_{0.90}Ce_{0.10}FeO_3$ and $Bi_{0.90}Tb_{0.10}FeO_3$ (88.5% and 82.6%) compared with the absence of MF. A significant upward trend in the photocatalytic degradation ability of organic pollutant were noticed as 97.8% and 94.8% for $Bi_{1-x}R_xFeO_3$ (R = Ce, Tb; x = 0.10) at 0.5T of MF. However, the decrement in degradation were observed at 0.7T as 89.1 and 85.9%. These results suggest the optimum MF to achieve higher photocatalytic efficiencies is 0.5T, which retards the recombination of charge carriers and improves carrier transport to the surface.

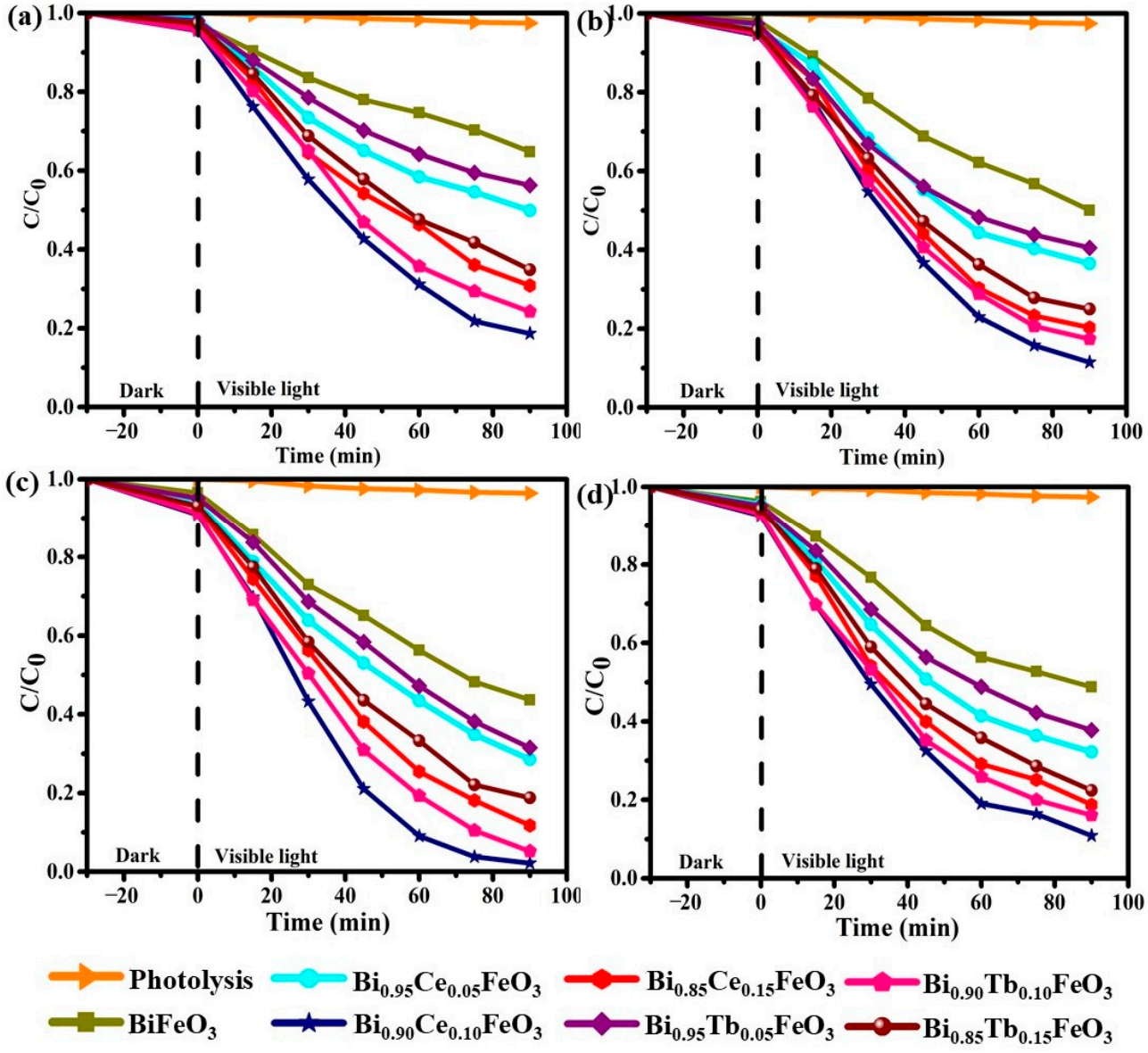

Figure 6. Photocatalytic degradation efficiencies of $Bi_{1-x}R_xFeO_3$ (R = Ce, Tb; x = 0.00, 0.05, 0.10 and 0.15) at (**a**) 0.0T (**b**) 0.3T (**c**) 0.5 T and (**d**) 0.7T of external MF.

Table 1. Photodegradation and Mineralization efficiencies of PR over BFO: RE nanostructures at different magnetic fields.

Sample	Photodegradation Efficiencies (%)				Mineralization Efficiencies (%)			
	@0.0T	@0.3T	@0.5T	@0.7T	@0.0T	@0.3T	@0.5T	@0.7T
$BiFeO_3$	35.2	49.9	56.4	51.2	29.9	45.5	50.3	48.1
$Bi_{0.95}Ce_{0.05}FeO_3$	50.2	63.4	71.5	67.8	44.2	53.9	66.2	60.6
$Bi_{0.90}Ce_{0.10}FeO_3$	81.3	88.5	97.8	89.1	75.1	82.0	92.4	83.7
$Bi_{0.85}Ce_{0.15}FeO_3$	69.1	79.7	88.2	81.2	61.8	72.6	81.9	73.5
$Bi_{0.95}Tb_{0.05}FeO_3$	43.7	59.4	68.5	62.2	40.4	51.2	60.8	55.5
$Bi_{0.90}Tb_{0.10}FeO_3$	75.7	82.6	94.8	85.9	69.1	77.1	89.2	80.3
$Bi_{0.85}Tb_{0.15}FeO_3$	65.1	75.0	81.2	77.6	57.6	67.2	75.0	70.9

The enhancement in catalytic activity by applying the external magnetic fields can be ascribed to the manifestation of the magneto-hydrodynamic effect (MHD) [34], where the magnetic convection can be attributed to the effective Lorentz force [50] on charged species. This force may help to modify the scavenging rates of the excited electrons and separate the oppositely charged species efficiently, which generates more hydroxyl radicals to oxidize PR leads to higher degradation efficiencies in the presence of the external MF. Apart from this, the spin-state mixing can be affected by the MF explained through Δg mechanism [27]. According to the ΔgM, the MFs influence the spin conversion between S and T states of a radical pair [51,52]. The geminated singlet pairs of electrons and holes produced by irradiation, can recombine with one another. By applying the MFs, the singlet pairs of charge carriers undergo spin state mixing to produce triplet pairs, that cannot recombine. Thus, the increased yield of triplet pairs escape from the pairs and reacts with PR anion and cation radicals on the surface of the semiconductor, leads to enhancement in the catalytic activity at 0.3 and 0.5T of applied MFs. However, the observed decreased photocatalytic activity at MF of 0.7T, indicates that spin-state mixing can be blocked by higher MFs and accelerates the recombination of electrons and holes if the present MF-effects occur during the re-encounter of free radicals [53]. At high MFs, the free radical activity may decrease by shifting the triplet to singlets and participate in the recombination from the s-pairs, which is much faster than the escape process. i.e., triplet pairs can disappear by the recombination process instead of the escape one and decreases the efficiency of PR degradation.

The PR degradation kinetics by BFO:RE nanostructures followed a pseudo-first-order reaction kinetics [54] shown in Figure 7a–d. The rate constants (k) were determined from the slope of the $ln(C/C_0)$ versus time (t), and tabulated in Table 2, signifies the enhanced catalytic activity was noticed at 0.5T for x = 0.10 in both the cases of RE substitution.

Figure 8 shows the mineralization efficiencies of PR by BFO: RE nanostructures under different MFs. The obtained values for the mineralization degradation and their corresponding degradation efficiencies were tabulated in Table 1. For the composition x = 0.10, observed the highest mineralization efficiencies of 92.4% and 89.2% for BFO: Ce and BFO: Tb nanostructures at 0.5T of the MF, confirms no aromatic rings of organic carbon left and the effectiveness in degrading the PR during photocatalytic experiments.

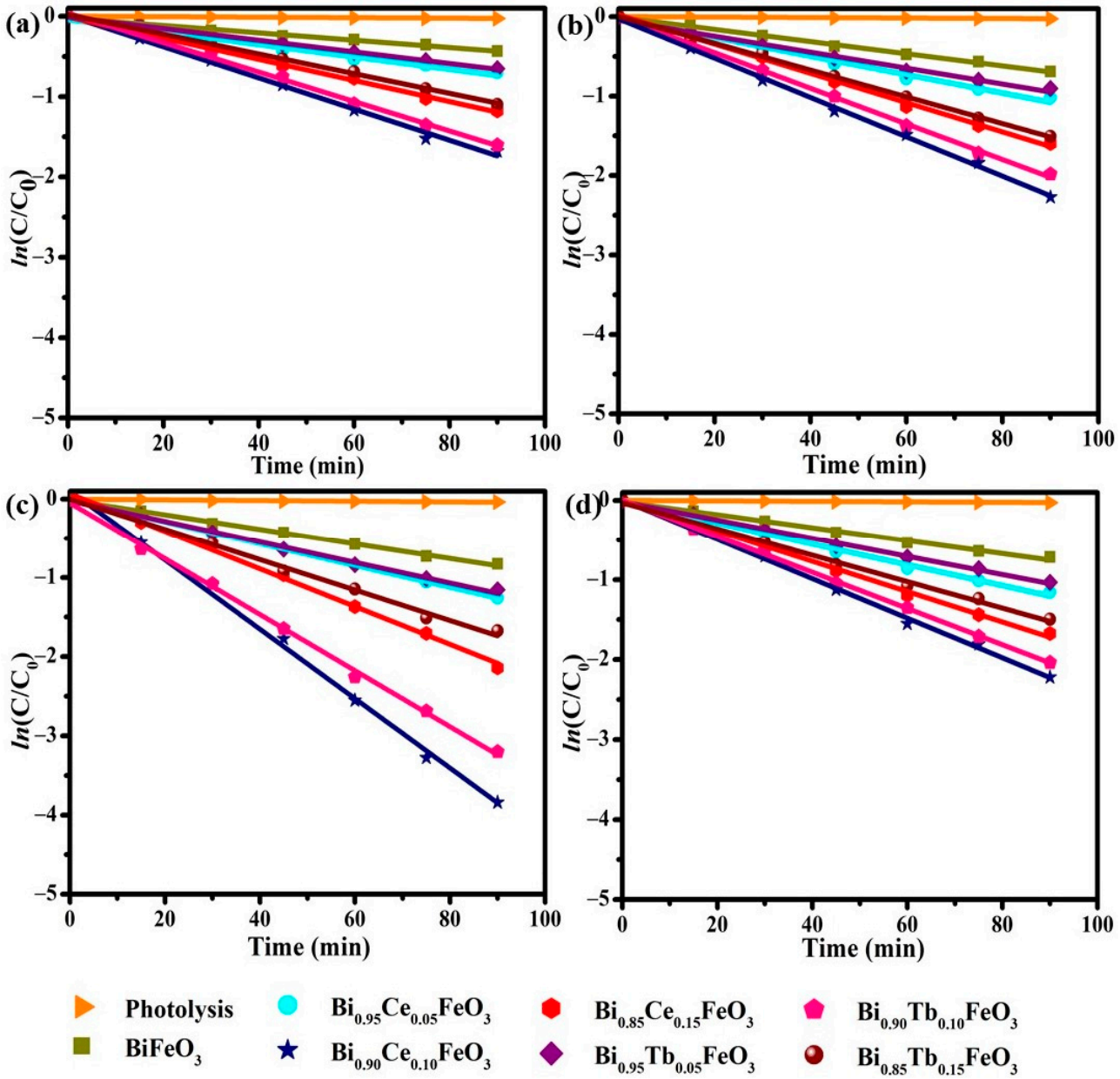

Figure 7. Photodegradation kinetics of $Bi_{1-x}R_xFeO_3$ (R = Ce, Tb; x = 0.00, 0.05, 0.10 and 0.15) nanostructures at (**a**) 0.0T (**b**) 0.3T (**c**) 0.5T and (**d**) 0.7T of MF.

Table 2. First-order reaction rate constants (*k*) at different magnetic fields for BFO: RE nanostructures.

Sample	@0.0T		@0.3T		@0.5T		@0.7T	
	R^2	k ($min^{-1} \times 10^{-3}$)	R^2	k ($min^{-1} \times 10^{-3}$)	R^2	k ($min^{-1} \times 10^{-3}$)	R^2	k ($min^{-1} \times 10^{-3}$)
$BiFeO_3$	0.98	4.5	0.99	7.6	0.99	9.2	0.99	8.1
$Bi_{0.95}Ce_{0.05}FeO_3$	0.97	7.6	0.98	11.6	0.99	13.7	0.99	12.9
$Bi_{0.90}Ce_{0.10}FeO_3$	0.99	19.4	0.99	24.7	0.99	43.8	0.99	28.7
$Bi_{0.85}Ce_{0.15}FeO_3$	0.99	13.1	0.99	18.4	0.99	23.9	0.98	19.0
$Bi_{0.95}Tb_{0.05}FeO_3$	0.99	7.2	0.98	10.0	0.99	13.0	0.99	11.4
$Bi_{0.90}Tb_{0.10}FeO_3$	0.99	18.3	0.99	22.4	0.99	35.4	0.97	23.6
$Bi_{0.85}Tb_{0.15}FeO_3$	0.99	12.2	0.99	16.8	0.99	19.3	0.98	17.1

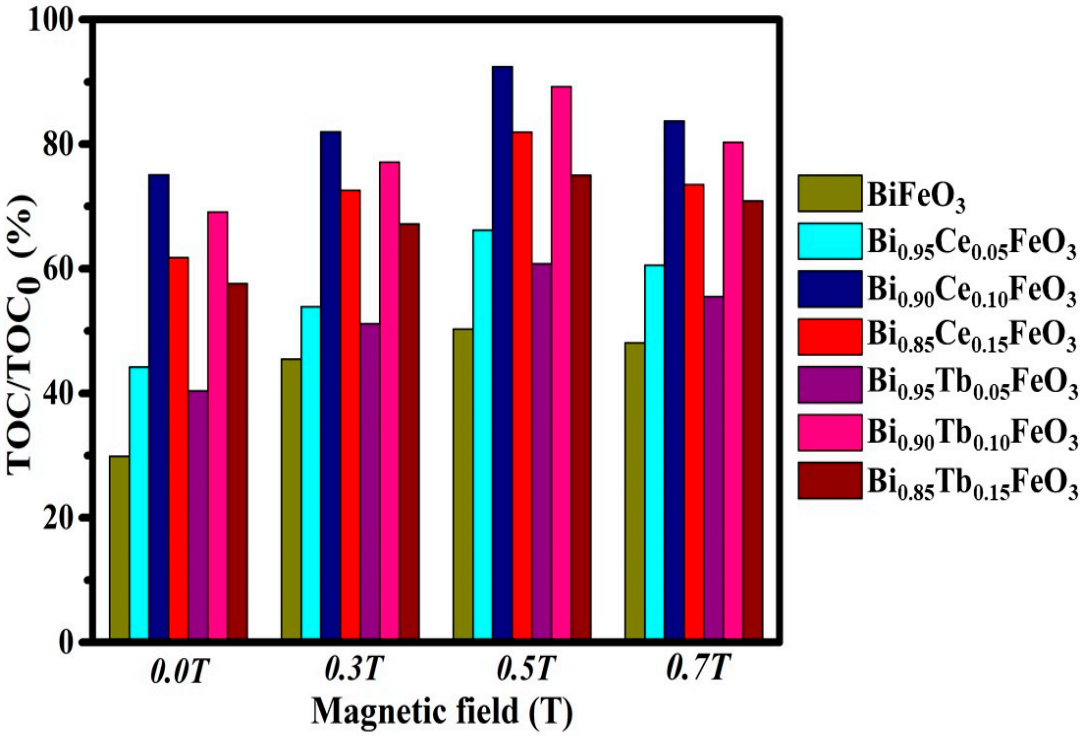

Figure 8. Mineralization efficiencies of BFO: RE nanostructures at different MFs.

Reproducibility is one of the tough issues in MF-assisted heterogeneous photocatalytic systems. To ensure the reproducibility, stability and reusability of BFO:RE, repetitive photodegradation studies were conducted for five consecutive cycles.

Figure 9a–d shows the efficiencies in the degradation of PR dye with an error less than 3% even after the five-sequential cycles, which validates the MF-assisted photocatalysis was certainly reproducible with highly reusable and stable BFO:Tb magnetic photocatalysts.

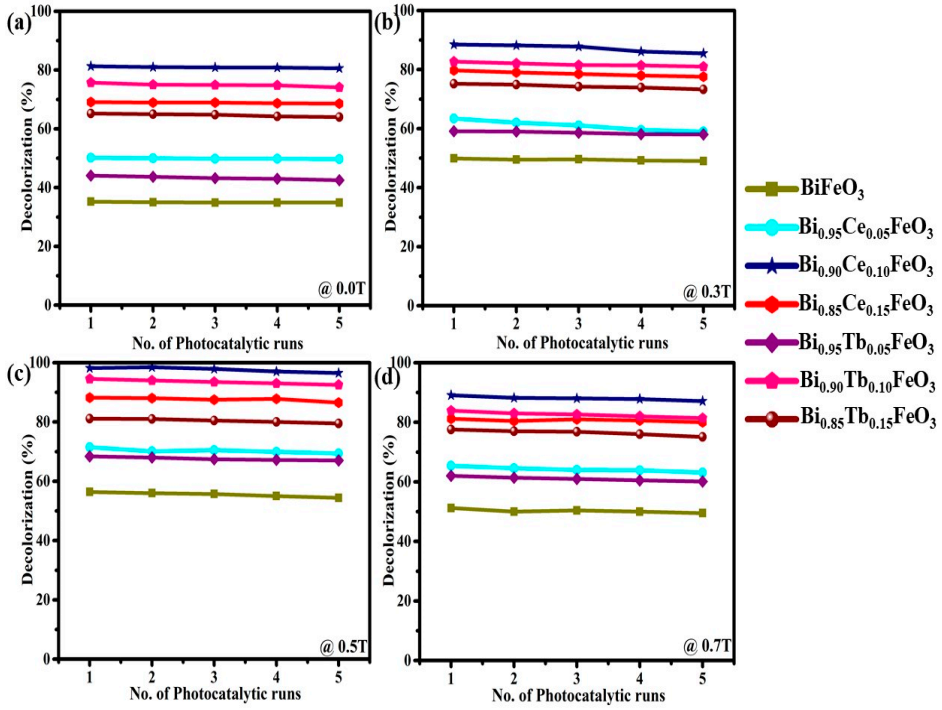

Figure 9. Recyclic degradation efficiencies of PR over BFO: RE nanostructures at (**a**) 0.0T (**b**) 0.3T (**c**) 0.5T (**d**) 0.7T of MF.

4. Conclusions

In summary, BFO: RE nanostructures were synthesized by the hydrothermal method. All the prepared samples were showed a nano-rod-like morphology, confirmed from the HR-TEM images. The structural studies showed the substitution induced structural transition from rhombohedral to orthorhombic with increasing the concentration of RE to BFO. The studies on the bandgap revealed that bandgap of the RE substituted BFO nanostructures decreased with increasing concentration of RE content. The enhanced magnetic properties were observed in BFO: RE nanostructures due to the substitution induced suppression of cycloidal spin structure. The investigations on photocatalytic studies revealed an enhanced photodegradation of PR was observed by applying the external magnetic field of 0.5T for the composition x = 0.10 in both the cases. The degradation raised to 97.8, 94.8% as magnetic strength increases from 0.0 to 0.5T and falls to 89.1%, 85.9% for 0.7T for $Bi_{1-x}R_xFeO_3$ (R = Ce, Tb; x = 0.10), respectively. The enhanced degradation of PR in MF is attributed to magnetically stimulated hindering the recombination of photo-generated charge carriers. The recyclable tests were confirmed the prepared BFO: RE nanostructures are highly reusable, and the MF-assisted catalytic systems were reproducible.

Author Contributions: Investigation, R.D.; data curation, writing-original draft preparation, R.D. and N.V.G.; Supervision, N.V.G. and J.C.D.; funding acquisition, J.C.D. All authors have read and agreed to the published version of the manuscript.

Funding: This research was funded by ANID/FONDECYT Postdoctoral Research Project No.: 3190134 and Basal CEDENNA AFB180001.

Institutional Review Board Statement: Not applicable.

Informed Consent Statement: Not applicable.

Data Availability Statement: Data can be made available upon reasonable request.

Conflicts of Interest: The authors declare no conflict of interest.

References

1. Yin, L.; Mi, W. Progress in $BiFeO_3$-Based Heterostructures: Materials, Properties and Applications. *Nanoscale* **2020**, *12*, 477–523. [CrossRef]
2. Haruna, A.; Abdulkadir, I.; Idris, S.O. Photocatalytic Activity and Doping Effects of $BiFeO_3$ Nanoparticles in Model Organic Dyes. *Heliyon* **2020**, *6*, e03237. [CrossRef] [PubMed]
3. Gao, F.; Chen, X.Y.; Yin, K.B.; Dong, S.; Ren, Z.F.; Yuan, F.; Yu, T.; Zou, Z.G.; Liu, J.-M. Visible-Light Photocatalytic Properties of Weak Magnetic $BiFeO_3$ Nanoparticles. *Adv. Mater.* **2007**, *19*, 2889–2892. [CrossRef]
4. Gao, T.; Chen, Z.; Huang, Q.; Niu, F.; Huang, X.; Qin, L.; Huang, Y. A Review: Preparation of Bismuth Ferrite Nanoparticles and Its Applications in Visible-Light Induced Photocatalysis. *Rev. Adv. Mater. Sci.* **2015**, *40*, 97–109.
5. Lam, S.-M.; Sin, J.-C.; Mohamed, A.R. A Newly Emerging Visible Light-Responsive $BiFeO_3$ Perovskite for Photocatalytic Applications: A Mini Review. *Mater. Res. Bull.* **2017**, *90*, 15–30. [CrossRef]
6. Chen, X.; Mao, S.S. Titanium Dioxide Nanomaterials: Synthesis, Properties, Modifications, and Applications. *Chem. Rev.* **2007**, *107*, 2891–2959. [CrossRef]
7. Zhang, H.; Chen, G.; Bahnemann, D.W. Photoelectrocatalytic Materials for Environmental Applications. *J. Mater. Chem.* **2009**, *19*, 5089–5121. [CrossRef]
8. Rong, N.; Chu, M.; Tang, Y.; Zhang, C.; Cui, X.; He, H.; Zhang, Y.; Xiao, P. Improved Photoelectrocatalytic Properties of Ti-Doped $BiFeO_3$ Films for Water Oxidation. *J. Mater. Sci.* **2016**, *51*, 5712–5723. [CrossRef]
9. Senne, J.K. Electrochemical and Nuclear Magnetic Resonance Spectroscopy Studies of Phenol Red and Related Compounds. Ph.D. Thesis, Lowa State University, Ames, IA, USA, 1969.
10. Senne, J.K.; Marple, L.W. Electrochemical Reduction of Phenol Red. *Anal. Chem.* **1970**, *42*, 1147–1150. [CrossRef]
11. Thanasekaran, P.; Rajendran, T.; Rajagopal, S.; Srinivasan, C.; Ramaraj, R.; Ramamurthy, P.; Venkatachalapathy, B. Marcus Inverted Region in the Photoinduced Electron Transfer Reactions of Ruthenium(II)-Polypyridine Complexes with Phenolate Ions. *J. Phys. Chem. A* **1997**, *101*, 8195–8199. [CrossRef]
12. Li, C.; Hoffman, M.Z. One-Electron Redox Potentials of Phenols in Aqueous Solution. *J. Phys. Chem. B* **1999**, *103*, 6653–6656. [CrossRef]
13. Sires, I.; Guivarch, E.; Oturan, N.; Oturan, M.A. Efficient Removal of Triphenylmethane Dyes from Aqueous Medium by In Situ Electrogenerated Fenton's Reagent at Carbon-Felt Cathode. *Chemosphere* **2008**, *72*, 592–600. [CrossRef] [PubMed]

14. Yao, Y.; Liu, W.; Chan, Y.; Leung, C.; Mak, C.; Ploss, B. Studies of Rare-Earth Doped $BiFeO_3$ Ceramics. *Int. J. Appl. Ceram. Technol.* **2011**, *8*, 1246–1253. [CrossRef]
15. Hou, Y.; Qu, J.; Zhao, X.; Lei, P.; Wan, D.; Huang, C.P. Electro-Photocatalytic Degradation of Acid Orange II Using A Novel TiO_2/ACF Photoanode. *Sci. Total Environ.* **2009**, *407*, 2431–2439. [CrossRef] [PubMed]
16. Sekine, Y.; Tomioka, M.; Matsukata, M.; Kikuchi, E. Catalytic Degradation of Ethanol in An Electric Field. *Catal. Today* **2009**, *146*, 183–187. [CrossRef]
17. Jara, C.C.; Fino, D.; Spinelli, P. Bio-Refractory Organics Degradation over Semiconductor Foam under A Superimposed Electric Field. *Catal. Today* **2007**, *124*, 273–279. [CrossRef]
18. Aragones, A.C.; Haworth, N.L.; Darwish, N.; Ciampi, S.; Bloomfield, N.J.; Wallace, G.G.; Diez-Perez, I.; Coote, M.L. Electrostatic Catalysis of A Diels–Alder Reaction. *Nature* **2016**, *531*, 88–91. [CrossRef]
19. Yan, K.; Maark, T.A.; Khorshidi, A.; Sethuraman, V.A.; Peterson, A.A.; Guduru, P.R. The Influence of Elastic Strain on Catalytic Activity in the Hydrogen Evolution Reaction. *Angew. Chem. Int. Ed.* **2016**, *55*, 6175–6181. [CrossRef]
20. Wang, H.; Xu, S.; Tsai, C.; Li, Y.; Liu, C.; Zhao, J.; Liu, Y.; Yuan, H.; Abild-Pedersen, F.; Prinz, F.B.; et al. Direct and Continuous Strain Control of Catalysts with Tunable Battery Electrode Materials. *Science* **2016**, *354*, 1031–1036. [CrossRef]
21. Horikoshi, S.; Matsubara, A.; Takayama, S.; Sato, M.; Sakai, F.; Kajitani, M.; Abe, M.; Serpone, N. Characterization of Microwave Effects on Metal-Oxide Materials: Zinc Oxide and Titanium Dioxide. *Appl. Catal. B Environ.* **2009**, *91*, 362–367. [CrossRef]
22. Ai, Z.; Yang, P.; Lu, X. Degradation of 4-Chlorophenol by A Microwave Assisted Photocatalysis Method. *J. Hazard. Mater.* **2005**, *124*, 147–152. [CrossRef]
23. Entezari, M.H.; Heshmati, A.; Sarafraz-yazdi, A. A Combination of Ultrasound and Inorganic Catalyst: Removal of 2-Chlorophenol from Aqueous Solution. *Ultrasonics Sonochem.* **2005**, *12*, 137–141. [CrossRef] [PubMed]
24. Madhavan, J.; Kumar, P.S.S.; Anandan, S.; Grieser, F.; Ashokkumar, M. Sonophotocatalytic Degradation of Monocrotophos Using TiO_2 and Fe^{3+}. *J. Hazard. Mater.* **2010**, *177*, 944–949. [CrossRef] [PubMed]
25. Futamura, S.; Einaga, H.; Kabashima, H.; Hwan, L.Y. Synergistic Effect of Silent Discharge Plasma and Catalysts on Benzene Decomposition. *Catal. Today* **2004**, *89*, 89–95. [CrossRef]
26. Hao, X.L.; Zhou, M.H.; Lei, L.C. Non-Thermal Plasma-Induced Photocatalytic Degradation of 4-Chlorophenol in Water. *J. Hazard. Mater.* **2007**, *141*, 475–482. [CrossRef]
27. Steiner, U.E.; Ulrich, T. Magnetic Field Effects in Chemical Kinetics and Related Phenomena. *Chem. Rev.* **1989**, *89*, 51–147. [CrossRef]
28. Wakasa, M.; Suda, S.; Hayashi, H.; Ishii, N.; Okano, M. Magnetic Field Effect on the Photocatalytic Reaction with Ultrafine TiO_2 Particles. *J. Phys. Chem. B* **2004**, *108*, 11882–11885. [CrossRef]
29. Krenke, T.; Duman, E.; Acet, M.; Wassermann, E.F.; Moya, X.; Manosa, L.; Planes, A. Inverse Magnetocaloric Effect in Ferromagnetic Ni–Mn–Sn Alloys. *Nat. Mater.* **2005**, *4*, 450–454. [CrossRef] [PubMed]
30. Blaauw, C.; Woude, F.V.D. Magnetic and Structural Properties of $BiFeO_3$. *J. Phys. C Solid State Phys.* **1973**, *6*, 1422. [CrossRef]
31. Dhanalakshmi, R.; Vanga, P.R.; Ashok, M.; Giridharan, N.V. The Effect of A 0.5 T Magnetic Field on the Photocatalytic Activity of Recyclable Nd-modified $BiFeO_3$ Magnetic Catalysts. *IEEE Magn. Lett.* **2016**, *7*, 2106904. [CrossRef]
32. Kiwi, J. Magnetic Field Effects on Photosensitized Electron Transfer Reactions in the Presence of TiO_2 and CdS Loaded Particles. *J. Phys. Chem.* **1983**, *87*, 2274–2276. [CrossRef]
33. Wakasa, M.; Ishii, N.; Okano, M. Magnetic Field Effect on Photocatalytic Decomposition Reaction of Tert-Butanol with Platinized TiO_2 Particles. *C. R. Chim.* **2006**, *9*, 836–840. [CrossRef]
34. Okumura, H.; Endo, S.; Joonwichien, S.; Yamasue, E.; Ishihara, K.N. Magnetic Field Effect on Heterogeneous Photocatalysis. *Catal. Today* **2015**, *258*, 634–647. [CrossRef]
35. Li, J.; Pei, Q.; Wang, R.; Zhou, Y.; Zhang, Z.; Cao, Q.; Wang, D.; Mi, W.; Du, Y. Enhanced Photocatalytic Performance through Magnetic Field Boosting Carrier Transport. *ACS Nano* **2018**, *12*, 3351–3359. [CrossRef] [PubMed]
36. Dhanalakshmi, R.; Muneeswaran, M.; Vanga, P.R.; Ashok, M.; Giridharan, N.V. Photocatalytic Activity of BiFeO3 Nanoparticles Synthesized through Hydrothermal Method. *AIP Conf. Proc.* **2015**, *1665*, 130014.
37. Dhanalakshmi, R.; Muneeswaran, M.; Vanga, P.R.; Ashok, M.; Giridharan, N.V. Enhanced Photocatalytic Activity of Hydrothermally Grown $BiFeO_3$ Nanostructures and Role of Catalyst Recyclability in Photocatalysis Based on Magnetic Framework. *Appl. Phys. A* **2016**, *122*, 13. [CrossRef]
38. Dhanalakshmi, R.; Muneeswaran, M.; Shalini, K.; Giridharan, N.V. Enhanced Photocatalytic Activity of La-Substituted $BiFeO_3$ Nanostructures on the Degradation of Phenol Red. *Mater. Lett.* **2016**, *165*, 205–209. [CrossRef]
39. Bhushan, B.; Wang, Z.; Tol, J.V.; Dalal, N.S.; Basumallick, A.; Vasanthacharya, N.Y.; Kumar, S.; Das, D. Tailoring the Magnetic and Optical Characteristics of Nanocrystalline $BiFeO_3$ by Ce Doping. *J. Am. Ceram. Soc.* **2012**, *95*, 1985–1992. [CrossRef]
40. Arora, M.; Kumar, M. Structural, Magnetic and Optical Properties of Ce Substituted $BiFeO_3$ Nanoparticles. *Ceram. Int.* **2015**, *41*, 5705–5712. [CrossRef]
41. Lotey, G.S.; Verma, N.K. Multiferroic Properties of Tb-Doped $BiFeO_3$ Nanowires. *J. Nanopart. Res.* **2013**, *15*, 1553. [CrossRef]
42. Simoes, A.Z.; Stojanovic, B.D.; Ramirez, M.A.; Cavalheiro, A.A.; Longo, E.; Varela, J.A. Lanthanum-Doped $Bi_4Ti_3O_{12}$ Prepared by the Soft Chemical Method: Rietveld Analysis and Piezoelectric Properties. *Ceram. Int.* **2008**, *34*, 257–261. [CrossRef]
43. Gabbasova, Z.V.; Kuz'min, M.D.; Zvezdin, A.K.; Dubenko, I.S.; Murashov, V.A.; Rakov, D.N.; Krynetsky, I.B. $Bi_{1-x}R_xFeO_3$ (R=rare earth): A Family of Novel Magnetoelectrics. *Phys. Lett. A* **1991**, *158*, 491–498. [CrossRef]

44. Muneeswaran, M.; Jegatheesan, P.; Giridharan, N.V. Synthesis of Nanosized $BiFeO_3$ Powders by Co-Precipitation Method. *J. Exp. Nanosci.* **2013**, *8*, 341–346. [CrossRef]
45. Liu, J.; Lu, Y.; Liu, J.; Yang, X.; Yu, X. Investigation of Near Infrared Reflectance by Tuning the Shape of SnO_2 Nanoparticles. *J. Alloy Compd.* **2010**, *496*, 261–264. [CrossRef]
46. Sakar, M.; Balakumar, S.; Saravanan, P.; Bharathkumar, S. Compliments of Confinements: Substitution and Dimension Induced Magnetic Origin and Band-Bending Mediated Photocatalytic Enhancements in $Bi_{1-x}Dy_xFeO_3$ Particulate and Fiber Nanostructure. *Nanoscale* **2015**, *7*, 10667–10679. [CrossRef] [PubMed]
47. Sakar, M.; Balakumar, S.; Saravanan, P.; Bharathkumar, S. Particulates vs. Fibers: Dimension Featured Magnetic and Visible Light Driven Photocatalytic Properties of Sc Modified Multiferroic Bismuth Ferrite Nanostructures. *Nanoscale* **2016**, *8*, 1147–1160. [CrossRef] [PubMed]
48. Dhir, G.; Lotey, G.S.; Uniyal, P.; Verma, N.K. Size-Dependent Magnetic and Dielectric Properties of Tb-Doped BiFeO3 Nanoparticles. *J. Mater. Sci. Mater. Electron.* **2013**, *24*, 4386–4392. [CrossRef]
49. Guo, R.; Fang, L.; Dong, W.; Zheng, F.; Shen, M. Enhanced Photocatalytic Activity and Ferromagnetism in Gd Doped $BiFeO_3$ Nanoparticles. *J. Phys. Chem. C* **2010**, *114*, 21390–21396. [CrossRef]
50. Wang, Y.-H.; Zhao, J.-L.; Liang, Y. Degradation kinetics of phenol by a titanium dioxide photocatalyst coupled with a magnetic field. *React. Kinet. Mech. Catal.* **2013**, *109*, 273–283. [CrossRef]
51. Gladkikh, V.S.; Burshtein, A.I. Double-Channel Recombination of the Radical Pairs via Incoherent Δg-Mechanism of Spin-Conversion. *Chem. Phys.* **2006**, *323*, 351–357. [CrossRef]
52. Veselov, A.V.; Melekhov, V.I.; Anisimov, O.A.; Molin, Y.N. The Induction of Quantum Beats by the Δg mechanism in Radical ion Pair Recombination. *Chem. Phys. Lett.* **1987**, *136*, 263–266. [CrossRef]
53. Nagakura, S.; Hayashi, H.; Azumi, T. *Dynamic Spin Chemistry: Magnetic Controls and Spin Dynamics of Chemical Reactions*, 1st ed.; Wiley: New York, NY, USA, 1998.
54. Wu, J.M.; Zhang, T.W. Photodegradation of Rhodamine B in Water Assisted by Titania Films Prepared through A Novel Procedure. *J. Photochem. Photobiol. A Chem.* **2004**, *162*, 171–177. [CrossRef]